

First Experimental Evidence of Amorphous Tin Oxide Formation in Lead-Free Perovskites by Spectroscopic Ellipsometry

Giovanni Mannino,* Jesús Sanchez-Diaz, Emanuele Smecca, Salvatore Valastro, Ioannis Deretzis, Rafael S. Sánchez, Juan P. Martinez-Pastor, Iván Mora-Seró,* and Alessandra Alberti

The most promising lead-free options for producing perovskite solar cells are tin halide perovskite materials. Herein, while in situ monitoring the optical evolution of the material in humid air, spectroscopic ellipsometry is used to investigate the dielectric function of FASnI₃ layers (with and without additives) within the range of 1–5 eV. According to calculations based on the density functional theory that shows oxygen diffusion on FASnI₃ surfaces, the steady decrease in absorption coefficient in the band gap region (1.47 eV) and simultaneous increase in absorption in the 3–4.5 eV region suggest the production of amorphous tin oxide. Concurrently, X-ray diffraction reveals a clear degradation of FASnI₃. With the addition of sodium borohydride and dipropylammonium iodide, the optically active area of about 1.47 eV is preserved for a longer period while SnO₂ production is prevented. Last but not least, FASnI₃'s stability is investigated in dry N₂ environment and shown that it is optically durable for thermal operations up to 100 °C, particularly when additives are used.

1. Introduction


Tin halide perovskites (Sn-HPs) belong to the second class of halide perovskite materials with an ABX₃ stoichiometry that could potentially be used in light-harvesting devices, which show two main differences compared to their lead-based counterparts: 1) an increased environmental sustainability due to the absence of lead in their crystal structure, and 2) the presence of tunable band gaps with an energy range between 1.1 and 1.5 eV for the iodide structures (based on the choice of the A-site cation),^[1] thus enabling to access a solar spectral range not covered by lead-based derivatives. This last aspect is also exploitable for the realization of all-perovskite tandem solar architectures, as recently claimed in NREL's recent achievement of 25.5% efficiency.^[2]

However, the presence of a metallic element with facile oxidation, from the Sn²⁺ to the Sn⁴⁺ state, not only compromises the desired electro-optical properties and robustness of the Sn-HP structures but also promotes the formation of competitive phases like A₂SnI₆ or SnI₄, which indeed limit their application scope. Despite the recent advances in lead-free perovskites (LFPs), with a particular focus on Sn-HP derivatives,^[3–5] a full understanding of the degradation mechanisms, the effect of the very often incorporated additives and the influence of the generated byproducts is still missing. In addition, state-of-the-art Sn-HP solar cells are experiencing a continuous increase in the last years,^[6–8] reaching currently photoconversion efficiencies higher than 14%,^[9] but being far below the lead-based counterparts. Apart from the need of circumventing the inherent limitations and challenges that Sn-HP show, that is, 1) poor film morphology due to the rapid crystallization, 2) unsuitable energy level alignment and/or incompatibility with commonly used charge selective contacts, and 3) limited long-term stability and high p-doping levels due to the facile oxidation of divalent Sn²⁺ into Sn⁴⁺, big efforts must be also dedicated to the optimization of the architecture of devices to enhance the light-absorption and/or emission for the fabrication of more efficient solar cells and/or light-emitting diodes (LEDs),^[10–12] respectively, generation of amplified spontaneous emission (ASE) for low-cost

G. Mannino, E. Smecca, S. Valastro, I. Deretzis, A. Alberti
National Research Council (CNR)
Institute for Microelectronics and Microsystems (IMM)
Zona Industriale Strada VIII No. 5, 95121 Catania, Italy
E-mail: giovanni.mannino@imm.cnr.it

J. Sanchez-Diaz, R. S. Sánchez, I. Mora-Seró
Institute of Advanced Materials (INAM)
Universitat Jaume I
Av. Sos Baynat, s/n, 12071 Castello, Spain
E-mail: sero@uji.es

J. P. Martinez-Pastor
UMDO
Instituto de Ciencia de los Materiales
Universidad de Valencia
c/Catedrático J. Beltrán, 2, 46980 Paterna, Spain

 The ORCID identification number(s) for the author(s) of this article can be found under <https://doi.org/10.1002/solr.202300610>.

© 2023 The Authors. Solar RRL published by Wiley-VCH GmbH. This is an open access article under the terms of the Creative Commons Attribution License, which permits use, distribution and reproduction in any medium, provided the original work is properly cited.

DOI: 10.1002/solr.202300610

and high-quality lasers,^[13] development of devices for communications.^[14] Photonics has shown to be a powerful discipline for such purposes, but the suitable optimization of the photonic structures for each particular case requires a previous full characterization of the photophysical properties and parameters of the light-active material, that is, perovskite, which are not always easily available. Within this context, in situ optical measurements could, on the one hand, shed light on the changes in the light-absorption properties of Sn-HPs upon variation of the external conditions, for example, temperature or atmosphere composition, while monitoring the evolution of the dielectric properties of the materials, thus offering valuable details about the degradation pathways. On the other hand, an exhaustive characterization of Sn-HP semiconductors provide photophysical parameters, for example, absorption coefficient (α) over a broad spectral range, band gap (E_g) and interband transitions energies (E_x), which could be exploited for the implementation of photonic strategies.

In this article, we focus on the formamidinium (FA) based FASnI_3 perovskite, whose stability has recently been reported to be significantly improved by the use of an appropriate combination of additives.^[5] We perform spectroscopic ellipsometry measurements to study its optical properties (with and without additives) in the range of 1–5.5 eV. Using the critical point (CP) analysis, we precisely identify the energy band gap and the interband transitions at higher energies, which characterize the optical response of the non-degraded material. We observe the changes in the optical spectrum induced during material degradation, under humid air conditions, noticing the formation of a new CP at ≈ 3.6 eV that indicates a tin oxide phase (like SnO_2). This point is further corroborated by density functional theory calculations, which show facile oxygen diffusion even in thermodynamically stable FASnI_3 surfaces. We finally note that the formation of tin oxide has been hypothesized in some experiments but mainly during device operation.^[15–20] In this respect, our experiments focus on the degradation of the material by focusing on the pathway and mechanism of degradation of Sn-based perovskite material only.

2. Results and Discussion

Here, we report a detailed study of the absorption coefficient and refractive index of an Sn-HP derivative, that is, FASnI_3 , to identify their degradation pathways. Hence, before studying degradation, it is critical to know the optical constants of freshly generated samples in order to establish their reference profile for benchmarking purposes. With this aim, we used spectroscopic ellipsometry measurements over a wide range of wavelengths from 225 to 1240 nm (1–5.5 eV). With this method, Ψ and Δ , that is, the relative changes in amplitude and phase of the polarized light upon interaction with the perovskite layer, can be related to the dielectric function of the material, either on crystalline or amorphous lattices. The experimental wavelength-by-wavelength data were initially collected by loading the sample in a closed chamber filled with N_2 to prevent interaction with humid air. The enclosure allows data to be collected at only an angle of 70° . Experimental data and the model for FASnI_3 and $\text{FASnI}_3 + \text{DiPI} + \text{NaBH}_4$ (hereafter $\text{FASnI}_3 + \text{Add}$) samples, respectively, are shown in Figure 1a,b. All the collected data, including depolarized

components measured with an autoretarder setup, have been used to build a Kramers–Kronig consistent optical model. Seven Tauc-Lorentz oscillators have been used to describe asymmetrical band transitions and extract the dielectric function of the perovskite layers. It is worth pointing out that the number and type of oscillators were fixed, and the oscillator shift was the only parameter allowed to be modified for the correct fitting following an iterative minimization of the mean square error. Under these conditions, the method applies equally to the two materials and describes them without introducing any artefacts. The fitting of Ψ and Δ data was done with minimal adjustment of parameters to adapt it to FASnI_3 and $\text{FASnI}_3 + \text{Add}$ samples (Figure 1a,b), respectively. Interestingly, a good match between the fitting model and the experimental results for both materials was obtained over the whole wavelength range investigated. Figure 1c,d shows the real (ϵ_1) and imaginary (ϵ_2) parts of the dielectric function extracted by the model of the two perovskite samples measured at room temperature in dry N_2 . The absorption coefficient (Figure 1e,f) can be calculated from the dielectric function according to Equation (1)

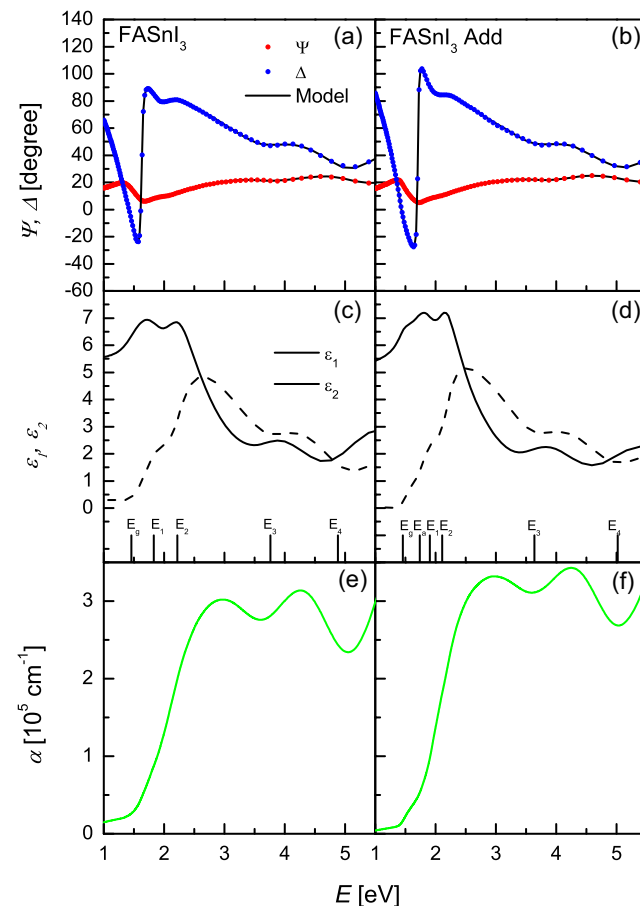


Figure 1. a,b) Spectroscopic ellipsometry measurements: experimental (symbols) and modeled (lines) curves at 70° angle of incidence for FASnI_3 and $\text{FASnI}_3 + \text{Add}$. E_g and E_{1-4} refer to interband transition energies obtained from CP analysis (see Equation (1) and (2)). c,d) Real (ϵ_1) and imaginary (ϵ_2) parts of the dielectric function as obtained from the modelling of ellipsometry data, e,f) Absorption coefficient derived from the dielectric function (see Equation (3)).

$$\alpha = \frac{2\omega}{c} \sqrt{\frac{\sqrt{(\epsilon_1^2 + \epsilon_2^2)} - \epsilon_1}{2}} \quad (1)$$

where ϵ_1 and ϵ_2 are obtained from the optical model, ω is the frequency of the light and c is the speed of light.^[21,22]

An important feature to be discussed is the region below the band gap, where the material should, in principle, be transparent. Therein, the low value of the absorption coefficient testifies the high optical quality of the materials. Remarkably, the presence of additives, likely located at the grain boundaries or eventually at the surface, not only induced a lower absorption tail in the sub-bandgap region, thus evidencing their beneficial effect in minimizing the formation of defects, but also enhanced the absorption coefficient above 2.5 eV.

An accurate determination of the band gap value is obtained using the CP analysis theory developed by Cardona, Aspnes and Lynch.^[23–26] This analysis relies on the densities of states of electron and phonon bands that possess singularities corresponding to CPs in the dielectric function. Materials with a direct band gap have an interband CP at the fundamental absorption edge, which corresponds to the direct excitonic transition from the highest valence band to the lowest conduction band split-off (E_0) in the Brillouin zone. The structures observed in the $\epsilon(\omega)$ spectra are attributed to interband transitions, which can be analyzed in terms of standard analytic line shapes according to Equation (2)

$$\epsilon(\omega) = C - Ae^{i\Phi}(\omega - E + i\Gamma)^n \quad (2)$$

where a CP is described by its amplitude A , threshold energy E , the broadening Γ , and the excitonic phase angle Φ ; n is the singularity dimension.^[27–30] These points are better identified by calculating the second derivative of the measured dielectric function and finding the simultaneous best fit to the real and imaginary parts of the function using a least-square procedure to Equation (3)

$$\frac{\partial^2 \epsilon}{\partial \omega^2} = n(n-1)Ae^{i\Phi}(\omega - E + i\Gamma)^{(n-2)} \quad (3)$$

If the gap is a purely discrete excitonic transition, $n = -1$ and the excitonic phase $\Phi \neq 0$ (Fano profile).^[31,32] Figure S1, Supporting Information, displays the second derivatives with the fitting curves.

The transition energies are shown in Figure 1c,d as vertical markers starting from the energy of the gap (E_g) and those at higher energies (E_1, E_2, E_3, E_4). FASnI₃ and FASnI₃ + Add share an almost identical shape of the dielectric function except for the extra transition induced (E_a) by the presence of additives, which slightly modifies the dielectric function just above the gap between E_g and E_1 . The numerical values of all electronic transition energies are reported in Table 1.

After establishing the optical properties of the fresh as-prepared samples, we investigated the optical properties during degradation upon exposure to humid air (40%). For simplicity reasons, we only show the absorption coefficient as a result of the complete data analysis above discussed. Note that a full range measurement lasts 12 min, and the overall measurement takes 16 h (960 min) for a total of 80 measurements on each layer, which allows to follow carefully any trend. For this purpose, once

Table 1. Interband transition energies as extracted from CP analysis for FASnI₃ and FASnI₃ + add layers analyzed at room temperature in an N₂ environment.

	FASnI ₃	FASnI ₃ + Add
E_g	1.45 ± 0.03	1.46 ± 0.03
E_a	–	1.74 ± 0.05
E_1	1.83 ± 0.05	1.90 ± 0.05
E_2	2.21 ± 0.08	2.11 ± 0.07
E_3	3.7 ± 0.1	3.6 ± 0.1
E_4	4.9 ± 0.2	5.0 ± 0.2

aligned, we intentionally left the sample in the same position inside the cell for the whole set of measurements to ensure the highest measurement reproducibility.

The most informative profiles are shown in Figure 2. The presence of additives completely changes the degradation kinetics for the reference (w/o additives) perovskite in two respects. There are two key regions to look at: one is the near band gap located at 2 eV and the other is in the range of 3.5–4 eV. In the absence of additives, the band gap undergoes a blue shift much more rapidly and after 480 min, an increase of the absorption coefficient in the sub-gap region is observed, thus indicating the presence of defects.^[33] At the same time, the value of the absorption coefficient initially decreases in the whole range. After 480 min, a second trend emerges in the 3.5–4 eV region, where the absorption coefficient starts to increase. Other studies in the literature using spectroscopic ellipsometry on pure SnO₂ layers demonstrate the absorption edge of that material in this region. (see Figure S2, Supporting Information).^[34,35]

On the Contrary, despite the FASnI₃ + Add samples show a sudden decrease during the first 120 min, the absorption coefficient in the 3.5–4 eV range remains low, but rather stable, very likely because the formation of SnO₂ is partially or fully inhibited by the presence of the additives. Interestingly, even though the E_g of this material undergoes a blue shift, much fewer defects are formed. Note that the absorption coefficient of FASnI₃ goes near zero at the gap, but increases at lower energy values with increasing time, thus suggesting the formation of defects (Figure 2). In contrast, the formation of defects is delayed and less pronounced for FASnI₃ + Add samples. Though X-ray diffraction (XRD) measurements did not reveal the characteristic SnO₂ pattern upon exposure to humid air (Figure S3, Supporting Information), regardless of the presence or absence of additives, the high sensitivity of spectroscopic ellipsometry evidences its formation as a by-product of the oxidative degradation of FASnI₃, at least near the surface (given the high absorption coefficient at these energies).

By calculating the ratio between the absorption coefficient comprised within 3.5–4 eV and that of the 2–2.5 eV region, it is observed that SnO₂ forms faster and in higher amounts in the samples without additives (Figure 3), which demonstrates the beneficial role of additives towards enhancing the stability of LFP derivatives.

Using the CP analysis on all 80 measurements, the time dependence of each CP as a function of time was extracted, to

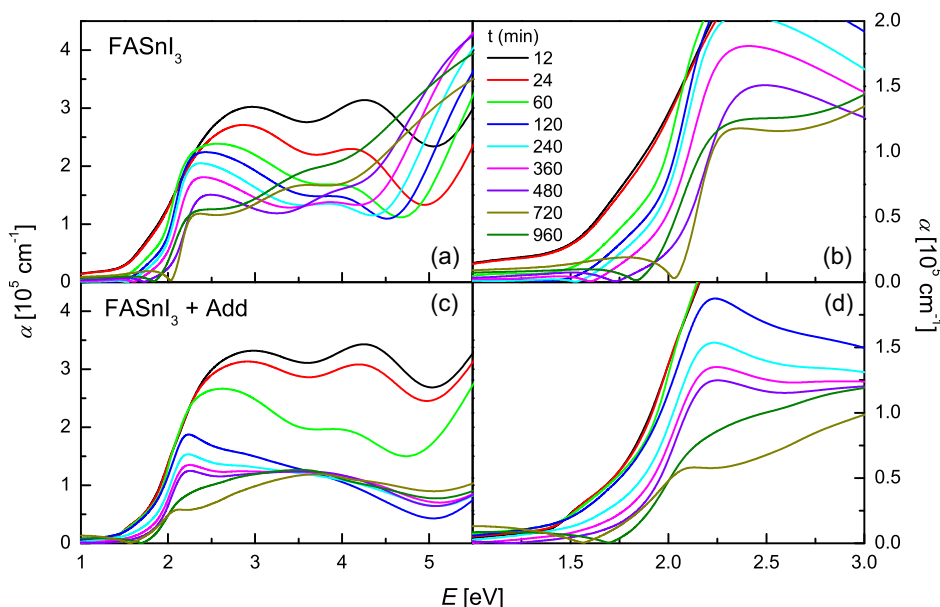


Figure 2. Absorption coefficient of a,b) FASnI₃ and c,d) FASnI₃ + Add as a function of exposure time to humid air.

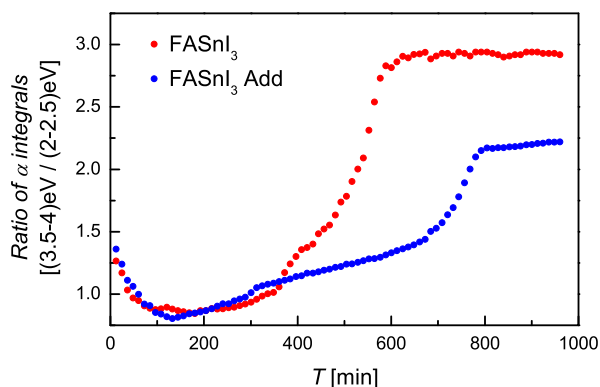


Figure 3. Ratio of integrals of the absorption coefficient as measured in two key regions: the Sn-HP and SnO₂ band gap regions, $E_g^{\text{Sn-HP}} \approx 2\text{--}2.5$ eV and $E_g^{\text{SnO}_2} \approx 3.5\text{--}4$ eV, respectively. In FASnI₃, the ratio increases at an earlier time and reaches higher values than in the FASnI₃ + Add sample.

quantify the layer degradation in humid air. Not all CPs are equally important because in some of them, the change is insignificant. **Figure 4a–c** shows data corresponding to the most important CPs present in the as-prepared material E_g (≈ 1.45 eV), E_1 (≈ 1.8 eV) and E_3 (≈ 3.7 eV) and one extra CP (E_{ox}) required to fit the experimental data when the SnO₂ signal appears, that is located at ≈ 3.5 eV. In addition to the energy, as previously demonstrated,^[36,37] the amplitude (see. Equation (2) and (3)) is an important parameter strictly related to the amount of material in a specific phase inside the layer. The amplitude of the above-mentioned CPs is shown in Figure 4b–d.

In the pristine FASnI₃ sample, (Figure 4a) the E_g CP lasts for only 100 min, after that time its amplitude is near zero (Figure 4b) and the CP at 1.8 eV (E_1) shifts to lower energy at 1.75 eV. This CP remains the only energy transition needed to describe the absorption edge with a constant amplitude. The

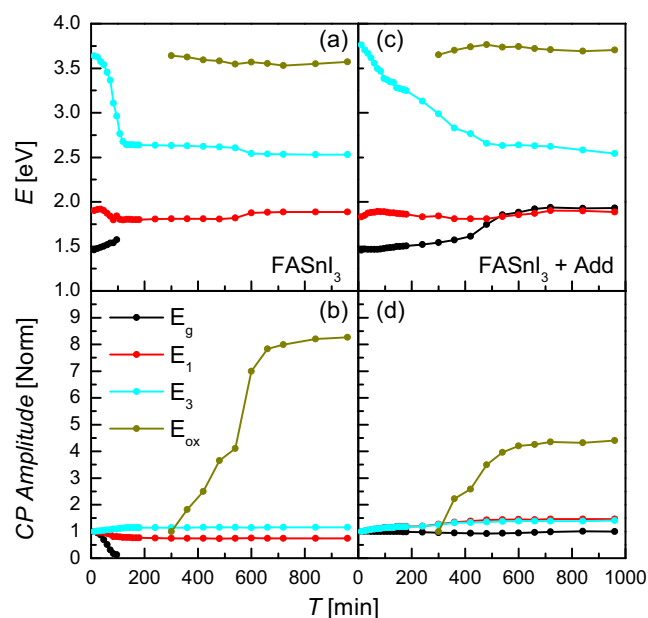


Figure 4. a,c) CP energy (E) and b,d) amplitude (A) of major interband transition as extracted from the fitting of Equation (3) for a,b) FASnI₃ and c,d) FASnI₃ + Add. The CP at E_g in FASnI₃ disappears faster (black dots) than in FASnI₃ + Add. SnO₂ CP (yellow dots) also appears at the same time, but the amplitude increases by a twofold factor for FASnI₃ compared to that of FASnI₃ + Add.

rapid blue shift is likely due to the p-doping effect due to the oxidation of Sn (Sn^{2+} to Sn^{4+}). A similar shift and amplitude behavior is observed in the CP located at 3.7 eV (E_3) on an identical timescale. After some time, this transition occurs, and that can be considered as a sample degradation, a CP (E_{ox}) at

3.5 eV appears (Figure 4a). The amplitude of this CP increases rapidly by eight times (Figure 4b), a significant value.

The just described picture is overall valid also for the $\text{FASnI}_3 + \text{Add}$ sample, but with three relevant differences: 1) the E_g CP does not vanish, and the sample absorption edge maintains both transitions at 1.46 and 1.90 eV (Figure 4c). A blue shift due to Sn^{+4} doping is observed, but at a more reduced rate. 2) The transition time that is, the capability of the sample to resist humid air, is extended by a fivefold factor, up to 500 min (Figure 4c) which is the time after which E_g and E_3 values become nearly constant. 3) The SnO_2 diagnostic CP at 3.5 eV appears at the same time for both kinds of samples (Figure 4a,c) but its intensity is decreased by a twofold factor compared to that reached for the samples without additives (Figure 4b,d).

To investigate the atomic-scale features of the oxidation process evidenced by the ellipsometry measurements, we calculated the diffusion barrier of O_2 molecules in FASnI_3 (001) surfaces and the subsequent oxidation of Sn. To this end, we used density functional theory (DFT) along with the climbing-image nudged elastic band method, considering thermodynamically stable FAI-terminated surfaces.^[38] The initial and the final images of the calculated minimum energy path were, respectively: 1) a physisorbed state for the O_2 molecule, which weakly interacts through van der Waals bonding with the FASnI_3 (001) surface, and 2) a chemisorbed state with the O_2 molecule being strongly bound to two Sn atoms of the surface. Figure 5 shows the respective initial and final configurations along with the minimum energy path that describes the diffusion of O_2 into the FASnI_3 surface. The energy levels of the initial and the final state in conjunction with the low values of the calculated energy barriers (0.11–0.12 eV) indicate that surface oxidation is strongly favorable. We note that the final oxidized state (chemisorbed state) has a 0.76 eV lower normalized energy than the initial physisorbed state.

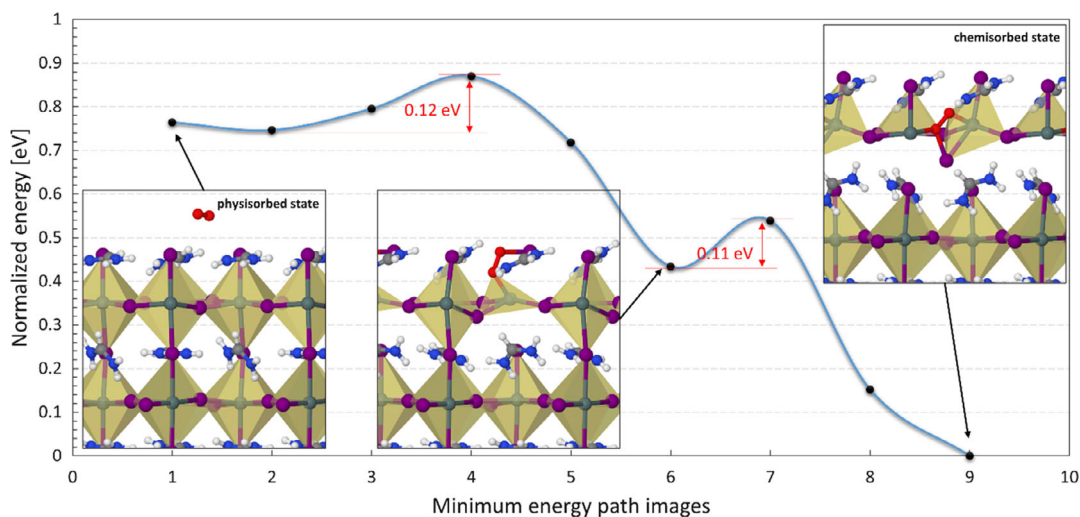


Figure 5. Calculation of diffusion for an O_2 molecule on a thermodynamically stable FASnI_3 (001) surface, showing the minimum energy path and the respective diffusion barriers. The initial configuration (left) shows a physisorbed O_2 molecule on the surface through van der Waals bonding, whereas the final configuration (right) indicates oxidation, as the O_2 molecule binds strongly with two Sn atoms of the FASnI_3 surface. The two diffusion barriers of the path have low values (0.11–0.12 eV) and the final energy has a lower value for the initial one, indicating an almost spontaneous surface oxidation process at room temperature.

We expect that in the case of other surface terminations with lower chemical stability as compared to the FAI-terminated surface, for example, the SnI_2 -terminated surface, oxidation at the surface should be a barrierless process. The above calculations indicate that oxygen diffusion should be quasispontaneous on FASnI_3 surfaces at room temperature, considering the low values of the calculated diffusion barriers. However, these calculations cannot rationalize whether this process is localized solely on FASnI_3 surfaces, or if it also propagates towards the bulk of the material.

Degradation at room temperature in air conditions is a process that irreversibly changes the perovskite layer composition, and it is likewise clear that the use of additives is beneficial to extend the stability of the perovskite layers in the ambient atmosphere. The intrinsic stability of FASnI_3 under interatmosphere of N_2

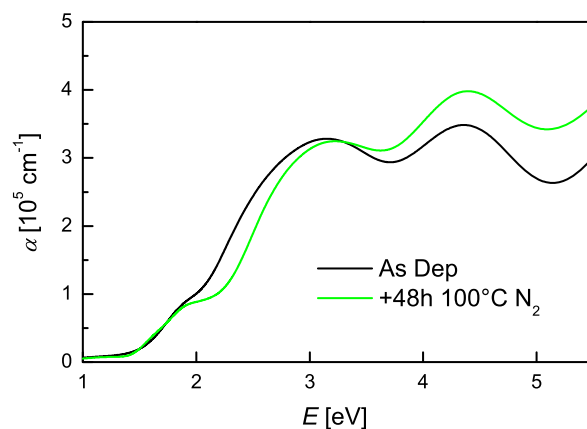


Figure 6. Absorption coefficient of FASnI_3 in N_2 environment at 100 °C. The inset shows the time evolution of the absorption coefficient in the region near the band gap to evidence the absence of defects inside the gap.

was examined as a step forward. As reported in the literature, nitrogen (N_2) can often contribute to extending the lifetime of materials.^[39–42] Ellipsometry measurements were indeed carried out in a closed chamber filled with N_2 using a preheating step at 100 °C (Figure 6). To highlight the possible beneficial effect of N_2 , we focused on $FASnI_3$ since it is more sensitive to environmental conditions; note that we have unambiguously demonstrated that $FASnI_3 + Add$ is much more robust than the pristine $FASnI_3$.^[5] Although the temperature is much higher

than that in the previous experiments and, in principle, more effective towards degradation, the absorption coefficient of $FASnI_3$ remains constant near the gap (and even increases in the UV region) in the absence of humidity, in contrast to the results with humid air (Figure 2). This further confirms that the main mechanism of $FASnI_3$ degradation is the Sn-O inter-action, rather than suffering from intrinsic thermal instability issues. The described scenario after the thermal heating in N_2 is consistent with previous data on $MAPbI_3$ perovskite.^[33]

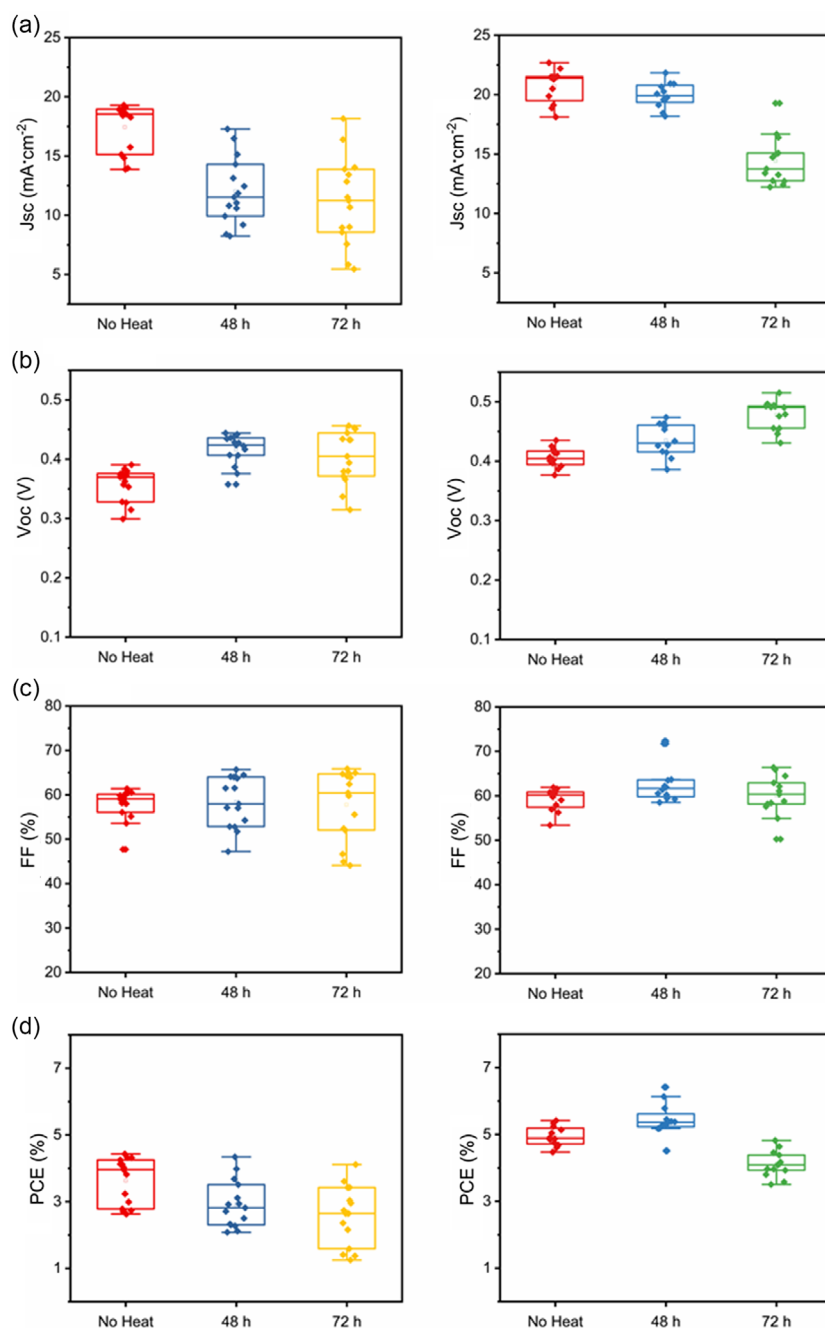


Figure 7. Cell parameters: a) J_{sc} , b) V_{oc} , c) FF, and d) PCE in a box-plot obtained from the J - V curves of $FASnI_3$ (left column) and $FASnI_3 + Add$ (right column). Each graph shows the evolution of the solar cells parameters after heating the glass/ITO/PEDOT:PSS/perovskite layers at 100 °C in N_2 for 48 and 72 h of thermal heating.

The effect of immersion in N_2 opens an interesting route to improve the realization of solar cells with a lead-free material and to provide more insights into this possibility. With this in mind, we fabricated solar cells with and without additives. The experiment was performed as described in the Experimental Section, in brief, the glass/ITO/PEDOT:PSS/Perovskite layers were exposed to heat stress for 0 (without thermal heating), 48, and 72 h of thermal heating at a constant temperature of 100 °C inside an N_2 -filled glovebox, before the deposition of the electron transport layer and electrode (C_{60} /BCP/Ag). As shown in from **Figure 7**, the power conversion efficiency (PCE) of the devices without additives decrease in the sample with 48 h of thermal heating, mainly due to a significant drop in the current density (J_{sc}). Instead, the PCE of those devices with additives increases upon 48 h of thermal heating; note that the J_{sc} remains constant during this period and after 72 h, a significant drop of the J_{sc} induces lessening efficiency. This variation seems to be directly correlated with the absorption of the films; as it is indicated in Figure S4a,c, Supporting Information, the absorption spectra of both films (with and without additives) increase in the region between 550 and 850 nm. In the case of the film without additives, the increase in the absorption is noted after 48 h of thermal heating whilst for the films with additives the onset is at 72 h of thermal heating, which is associated with the loss in the J_{sc} . This could be related with a thermal degradation on the bulk of $FASnI_3$ perovskite into side products such as FA_2SnI_6 or SnO_2 that is eventually delayed by the additive.^[4] Meanwhile, the open circuit voltage (V_{oc}) increases upon the heat stress, mainly attributed to the sublimation of SnI_4 that is located on the surface of the $FASnI_3$ film: as it was proved in other research works, SnI_4 starts sublimating at 100 °C.^[5] This helps to reduce the non-radiative recombination between the interfaces of the perovskite film with the charge selective contacts, as similarly reported for light soaking treatments.^[5] The best device we tested has $FF > 70\%$, PCE near 7%, V_{oc} around 0.45 V and J_{sc} above 20 mA cm^{-2} .

Overall, the characteristics of $FASnI_3 + Add$ compared to the control $FASnI_3$ samples leads us to highlight some outcomes on three different strata: 1) additives enhance the robustness of the material, even under high-temperature stress, whose benefits are extrapolated to the efficiency of solar cells with even improved electrical parameters; 2) inert environment is crucial to extend the electro-optical properties of $FASnI_3$ by preventing exposure to ambient moisture and oxidative degradation reactions; and 3) although intrinsic thermal degradation does not seem to be the main decomposition pathway of $FASnI_3$ semiconductors, our results point to the importance of optimizing the annealing time during the thermal heating to minimize premature degradation.

3. Conclusion

In conclusion, we have studied the degradation path of $FASnI_3$, an LFP derivative, and identified, through spectroscopic ellipsometry, the formation of amorphous SnO_2 that occurs in the early stage of the degradation process, which is not necessarily visible by other techniques. The energy transition values, which

reflect the band diagram shape, are now identified as a function time in both $FASnI_3$ and $FASnI_3 + Add$ for the first time in such a wide spectral range. While the sample is preserved in an inert environment, the absorption coefficient increases even at high temperatures. The use of additives (DipI and $NaBH_4$) in the preparation of the films, was crucial to perform this deep study as stability was prolonged and we could differentiate the degradation mechanisms. The long-term heat stress during the device fabrication, gives us insights about the intrinsic thermal degradation of the perovskite layer, depending on the thermal annealing time. Meanwhile, finding the correct annealing time could be beneficial to sublimate the SnI_4 located on the surface of the Sn -HP film, which helps to reduce the non-radiative recombination, thus increasing the V_{oc} .

4. Experimental Section

Materials: Tin (II) iodide (SnI_2 , 99.99%), bathocuproine (BCP, 99.99%), sodium borohydride ($NaBH_4$, 96%), *N, N*-dimethylformamide (DMF, 99.8%) and dimethylsulfoxide (DMSO, 99.8%) were purchased from Sigma-Aldrich. Tin (II) fluoride (SnF_2 , 97.5%) was purchased from Alfa Aesar and PEDOT: PSS 4083 aqueous solution was purchased from Heraeus. C_{60} (99.95%) was acquired from Nano-C. Formamidineum iodide (FAI, 99.99%) was purchased from Greatcell solar materials. All materials were used as received with no further purification.

Preparation of $FASnI_3$ Precursor Solutions: Samples were prepared following Ref. [5]. Briefly, Pristine $FASnI_3$ precursor solution: 298 mg of SnI_2 (0.8 M), 137.57 mg of FAI (0.8 M) and 12.48 mg of SnF_2 (0.08 M) were dissolved in 1 mL of a binary mixture of DMSO:DMF (9:1, v/v) and stirred overnight at room temperature.

$FASnI_3$ precursor solution with additives dipropylammonium iodide (DipI) and $NaBH_4$: 298 mg of SnI_2 (0.8 M), 123.81 mg of FAI (0.72 M), 36.65 mg of DipI (0.16 M), 12.48 mg of SnF_2 (0.08 M) and 0.1 mg of $NaBH_4$ (0.0026 M, may vary depending on the precursor purity, brand or Batch) were dissolved in 1 mL of a binary mixture of DMSO:DMF (9:1, v/v) and stirred overnight at room temperature.

Film Fabrication for Optical Study: The perovskite layer was deposited by a spin coating method, by adding $FASnI_3$ precursor solution (with or without additives) on top of a corning glass (2947) and spin-coated at 4000 rpm for the 50 s. Then 400 μ L of Chlorobenzene was dropped on top of the substrate after the 20 s of spinning, followed by a two-step annealing at 70 °C for 1 min and at 100 °C for 19 min. The process was done inside an N_2 -filled glovebox.

Device Fabrication: ITO-coated glass where chemically etched with zinc powder and HCl (6 M) to obtain the desired ITO pattern, followed by a sequential washing process with soap-water, ethanol, acetone and isopropanol, respectively, in an ultrasonic bath for 15 min each. Then, the substrates were dried with N_2 flow and subsequently introduced in a UV-ozone lamp for 20 min. The PEDOT:PSS solution was filtered with 0.45 μ m PVDF filter and spin-coated on top of ITO at 5000 rpm (2000 rpm s^{-1} of acceleration) for 40s and annealed at 130 °C for 20 min in ambient conditions. After the hole transporting layer (HTL) deposition, the substrates were introduced in a N_2 -filled glovebox, for the $FASnI_3$ layer deposition. The perovskite layer was deposited by a one-step method with an antisolvent-based method, by adding $FASnI_3$ precursor solution (with or without additives) on top of PEDOT:PSS and spin-coated at 4000 rpm for 50 s. Then 400 μ L of Chlorobenzene was dropped on top of the substrate after 20 s of spinning, followed by a two-step annealing at 70 °C for 1 min and at 100 °C for 19 min. A 30 nm layer of C_{60} was thermally evaporated on top of the perovskite layer as electron transporting layer (ETL), followed by 6 nm of BCP as a buffer layer and 100 nm of Ag as metal contact.

Thermal Heating Procedure: The overall device fabrication was performed as indicated in the device fabrication procedure, but in this case, the glass/ITO/PEDOT:PSS/Perovskite samples were exposed to a thermal

heating during 0 (without heating), 48, and 72 h of thermal heating, respectively, at a constant temperature of 100 °C using a hot-plate inside N₂ filled glovebox. The deposition of the top layers, that is, C₆₀/BCP/Ag, was performed by thermal evaporation following the standard procedures described above.

Ellipsometry Measurements: A J. A. Woollam VASE Ellipsometer was used to measure the changes in the optical constants. The ellipsometer was equipped with a rotating compensator, which allowed improved accuracy and a measure of the amount of non-polarized light, if present. The sample was kept in a closed chamber with an overpressure of N₂ to initially avoid sample degradation due to humid air. The cell setup allowed to vary the temperature in the range 30–100 °C with an Instec MK100 heater/cooler system with an accuracy of 0.1 °C. To establish a consolidated model, we measured the optical constants in the spectral range 1–5.5 eV. Being the sample deposited on glass, its presence was properly considered including the possibility that part of the light hits the back surface of the glass slide. The thickness of the perovskite, was determined by verifying that *n* obeys the Cauchy equation in the transparent region. This value was kept constant afterwards for assessing a Kramers-Kronig consistent optical model based on multiple CP parabolic band (CPPB)

X-Ray Diffraction Analysis: Analyses were performed using a Bruker AXS D8 Discover diffractometer equipped with a Cu-Kα source and high-precision goniometer (0.0001 Å) in a Bragg–Brentano configuration with a step size of 0.02° and a time/step of 10 s.

Density Functional Theory Calculations: Calculations were based on the density functional theory using the plane-wave Quantum Espresso software suite.^[43] We studied the chemisorption and diffusion of O₂ molecules on thermodynamically stable FAI-terminated FASnI₃ (001) surfaces using the recently developed vdW-DF3-opt1 van der Waals exchange-correlation functional along with Perdew–Burke–Ernzerhof ultrasoft pseudopotentials for the description of core electrons.^[44–46] Surface slabs containing three FA layers were constructed (1 bulk and 2 surface layers) interacting with a single O₂ molecule, having a lateral periodicity of 8.7 Å. A vacuum space of 15 Å was introduced along the surface direction to avoid spurious interactions between the periodic replicas of the system. Calculations were performed with a plane-wave cut-off kinetic energy of 46 Ry and an augmented charge density cutoff of 360 Ry. All atoms were allowed to fully relax. Finally, we used the climbing-image nudged elastic band method for the calculation of the diffusion barrier of O₂ within the FASnI₃ perovskite surface.^[47]

Supporting Information

Supporting Information is available from the Wiley Online Library or from the author.

Acknowledgements

The authors acknowledge the Mission Innovation Grant Agreement between the Italian Ministry of Ecological Transition and ENEA, Italian National Agency for New Technologies, Energy and Sustainable Economic Development (ref. agreement No. 21A03302 GU n.133 del 5-6-2021), CUP B82C21001820001. This work was partly supported by Horizon 2020 research and innovation program through the DROP-IT project (grant agreement No. 862656).

Conflict of Interest

The authors declare no conflict of interest.

Data Availability Statement

The data that support the findings of this study are available from the corresponding author upon reasonable request.

Keywords

absorption coefficients, dielectric functions, lead-free perovskites, perovskite solar cells, spectroscopic ellipsometry, tin halide perovskites

Received: August 3, 2023

Published online:

- [1] R. Prasanna, A. Gold-Parker, T. Leijtens, B. Conings, A. Babayigit, H.-G. Boyen, M. F. Toney, M. D. McGehee, *J. Am. Chem. Soc.* **2017**, *139*, 11117.
- [2] <https://www.nrel.gov/news/press/2022/new-additives-to-perovskite-tandem-solar-cells-boost-efficiency-stability.html> (accessed: June 2022).
- [3] Z. Zhang, X. Tian, C. Wang, J. Jin, Y. Jiang, Q. Zhou, J. Zhu, J. Xu, R. He, Y. Huang, S. Ren, C. Chen, P. Gao, R. Long, D. Zhao, *Energy Environ. Sci.* **2022**, *15*, 5274.
- [4] L. Lanzetta, T. Webb, N. Zibouche, X. Liang, D. Ding, G. Min, R. E. J. Westbrook, B. Gaggio, T. J. Macdonald, M. Saiful Islam, S. A. Haque, *Nat. Commun.* **2021**, *12*, 2853.
- [5] J. Sanchez-Diaz, R. F. Sánchez, S. Masi, M. Krečmarová, A. O. Alvarez, E. M. Barea, J. Rodriguez-Romero, V. S. Chirvony, J. F. Sánchez-Royo, J. Martínez-Pastor, I. Mora-Seró, *Joule* **2022**, *6*, 861.
- [6] C. Wang, F. Gu, Z. Zhao, H. Rao, Y. Qiu, Z. Cai, G. Zhan, X. Li, B. Sun, X. Yu, B. Zhao, Z. Liu, Z. Bian, C. Huang, *Adv. Mater.* **2020**, *32*, 1907623.
- [7] X. Liu, Y. Wang, T. Wu, X. He, X. Meng, J. Barbaud, H. Chen, H. Segawa, H. Yang, L. Han, *Nat. Commun.* **2020**, *11*, 2678.
- [8] T. Nakamura, S. Yakumaru, M. A. Truong, K. Kim, J. Liu, S. Hu, K. Otsuka, R. Hashimoto, R. Murdey, T. Sasamori, H. D. Kim, H. Ohkita, T. Handa, Y. Kanemitsu, A. Wakamiya, *Nat. Commun.* **2020**, *11*, 3008.
- [9] J. Zhou, M. Hao, Y. Zhang, X. Ma, J. Dong, F. Lu, J. Wang, N. Wang, Y. Zhou, *Matter* **2022**, *5*, 683.
- [10] S. Haque, M. Alexandre, C. Baretzky, D. Rossi, F. De Rossi, A. Vicente, F. Brunetti, H. Águas, R. Ferreira, E. Fortunato, M. Auf der Maur, U. Würfel, R. Martins, M. Mendes, *ACS Photonics* **2022**, *9*, 2408.
- [11] C. Cho, B. Zhao, G. Tainter, Y. Lee, R. Friend, D. Di, F. Deschler, N. Greenham, *Nat. Commun.* **2020**, *11*, 611.
- [12] V. Vescio, J. Sanchez-Diaz, J. Friero, R. Sánchez, S. Hernández, A. Cirera, I. Mora-Seró, B. Garrido *ACS Energy Lett.* **2022**, *7*, 3653.
- [13] V. Chirvony, I. Suárez, J. Sanchez-Diaz, R. Sánchez, J. Rodríguez-Romero, I. Mora-Seró, J. Martínez-Pastor *Adv. Mater.* **2023**, *35*, 2208293.
- [14] I. Suárez, V. Chirvony, J. Sánchez-Díaz, R. Sánchez, I. Mora-Seró, J. Martínez-Pastor, *Adv. Opt. Mater.* **2022**, *10*, 2200458.
- [15] D. Di Girolamo, E. Aktas, C. Ponti, J. Pascual, G. Li, M. Li, G. Nasti, F. Alharthi, F. Mura, A. Abate, *Mater. Adv.* **2022**, *3*, 9083.
- [16] J. Song, H. Liu, W. Pu, Y. Lu, Z. Si, Z. Zhang, Y. Ge, N. Li, H. Zhou, W. Xiao, L. Wang, M. Sui, *Energy Environ. Sci.* **2022**, *15*, 4836.
- [17] T. J. Macdonald, L. Lanzetta, X. Lian, D. Dong, S. A. Haque, *Adv. Mater.* **2023**, *35*, 2206684.
- [18] H. J. Jung, D. Kim, S. Kim, J. Park, V. P. Dravid, B. Shin, *Adv. Mater.* **2018**, *30*, 1802769.
- [19] H. Liu, Z. Zhang, W. Zuo, R. Roy, M. Li, M. M. Byranvand, M. Saliba, *Adv. Energy Mater.* **2023**, *13* 2202209.
- [20] S. Zhidkov, D. W. Boukhvalov, A. I. Kukharenko, L. D. Finkelstein, S. O. Cholakh, A. F. Akbulatov, E. J. Juarez-Perez, P. A. Troshin, E. Z. Kurmaev, *J. Phys. Chem. C* **2020**, *124*, 14928.
- [21] G. Mannino, I. Deretzis, E. Smecca, A. La Magna, A. Alberti, D. Ceratti, D. Cahen, *J. Phys. Chem. Lett.* **2020**, *11*, 2490.

- [22] G. Mannino, I. Deretzis, E. Smecca, F. Giannazzo, S. Valastro, G. Fiscaro, A. La Magna, D. Ceratti, A. Alberti, *J. Phys. Chem.* **2021**, 125, 4938.
- [23] M. Cardona, in *Modulation Spectroscopy Supplement 11 To Solid State Physics, Advances in Research and Applications*, Academic Press, Cambridge, MA **1969**.
- [24] M. Cardona, P. Yu, in *Fundamentals of Semiconductors, Physics and Materials Properties*, Springer-Verlag, Berlin **2010**.
- [25] D. E. Aspnes, in *Handbook on Semiconductors, Volume 2, Optical Properties of Solids*, North-Holland, Amsterdam **1980**.
- [26] D. W. Lynch, *Handbook of Optical Constants of Solids*, Academic Publishers, Cambridge, MA **1985**.
- [27] L. Vina, S. Logotheditis, M. Cardona, *Phys. Rev. B* **1984**, 30, 1979.
- [28] S. Logotheditis, L. Vina, M. Cardona, *Phys. Rev. B* **1985**, 31, 947.
- [29] P. Lautenschlager, M. Garriga, L. Vina, M. Cardona, *Phys. Rev. B* **1987**, 36, 4813.
- [30] P. Lautenschlager, M. Garriga, L. Vina, M. Cardona, *Phys. Rev. B* **1987**, 36, 4821.
- [31] U. Fano, *Phys. Rev.* **1961**, 124, 1866.
- [32] Y. Jiang, A. M. Soufiani, A. Gentle, F. Huang, A. Ho-Baillie, M. A. Green, *Appl. Phys. Lett.* **2016**, 108, 061905.
- [33] M. Losurdo, M. Bergmair, G. Bruno, D. Cattelan, C. Cobet, A. de Martino, K. Fleischer, Z. Dohcevic-Mitrovic, N. Esser, M. Galliet, R. Gajic, D. Hemzal, K. Hingerl, J. Humlicek, R. Ossikovski, Z. V. Popovic, O. Saxl, *J. Nanopart. Res.* **2009**, 11, 1521.
- [34] J. Gong, X. Wang, X. Fan, R. Dai, Z. Wang, Z. Zhang, Z. Ding, *Opt. Mat. Exp.* **2019**, 9, 3691.
- [35] F. Atay, V. Bilgin, I. Akyuz, E. Ketenci, S. Kose, *J. Non-Cryst. Solids* **2010**, 356, 2192.
- [36] S. Valastro, G. Mannino, E. Smecca, C. Bongiorno, S. Sanzaro, I. Deretzis, A. La Magna, A. K. Jena, T. Miyasaka, A. Alberti, *Sol. RRL* **2022**, 6, 2200008.
- [37] I. Deretzis, C. Bongiorno, G. Mannino, E. Smecca, S. Sanzaro, S. Valastro, G. Fiscaro, A. La Magna, A. Alberti, *Nanomaterials* **2021**, 11, 1282.
- [38] M. Pols, T. Hilpert, I. A. Filot, A. C. Van Duin, S. Calero, S. Tao, *ACS Appl. Mater. Interfaces* **2022**, 14, 40841.
- [39] G. Mannino, A. Alberti, I. Deretzis, E. Smecca, S. Sanzaro, Y. Numata, T. Miyasaka, A. La Magna, *J. Phys. Chem. C* **2017**, 121, 7703.
- [40] A. Alberti, E. Smecca, S. Sanzaro, G. Mannino, I. Deretzis, A. La Magna, *Rivista del Nuovo Cimento* **2019**, 42, 301.
- [41] A. Alberti, I. Deretzis, G. Mannino, E. Smecca, F. Giannazzo, A. Listorti, S. Colella, S. Masi, A. La Magna, *Adv. Energy Mater.* **2019**, 9, 1803450.
- [42] A. Alberti, C. Bongiorno, E. Smecca, I. Deretzis, A. La Magna, C. Spinella, *Nat. Commun.* **2019**, 10, 1.
- [43] P. Giannozzi, S. Baroni, N. Bonini, M. Calandra, R. Car, C. Cavazzoni, D. Ceresoli, L. C. Guido, M. Cococcioni, I. Dabo, A. D. Corso, S. de Gironcoli, S. Fabris, G. Fratesi, R. Gebauer, U. Gerstmann, C. Gougoussis, A. Kokalj, M. Lazzeri, L. Martin-Samos, N. Marzari, F. Mauri, R. Mazzarello, S. Paolini, A. Pasquarello, L. Paulatto, C. Sbraccia, S. Scandolo, G. Sclauzero, A. P. Seitsonen, et al., *J. Phys. Condens. Matter* **2009**, 21, 395502.
- [44] D. Chakraborty, K. Berland, T. Thonhauser, *J. Chem. Theory Comput.* **2020**, 16, 5893.
- [45] J. P. Perdew, K. Burke, M. Ernzerhof, *Phys. Rev. Lett.* **1996**, 77, 3865.
- [46] D. Vanderbilt, *Phys. Rev. B* **1990**, 41, 7892.
- [47] G. Henkelman, B. P. Uberuaga, H. Jónsson, *J. Chem. Phys.* **2000**, 113, 9901.